Isotope-Sensitive Imaging of Special Nuclear Materials Using Computer Tomography Based on Scattering Nuclear Resonance Fluorescence

Haoyang Lan,[1] Tan Song,[1] Zhuhua Luo,[2,3] Jianliang Zhou,[1,3] Zhichao Zhu,[1,3] and Wen Luo[1,3,*]

[1] *School of Nuclear Science and Technology, University of South China, Hengyang 421001, China*

[2] *School of Resources Environment and Safety Engineering, University of South China, Hengyang 421001, China*

[3] *National Exemplary Base for International Sci & Tech Collaboration of Nuclear Energy and Nuclear Safety, University of South China, Hengyang 421001, China*

(Received 5 August 2021; revised 12 October 2021; accepted 8 November 2021; published 29 November 2021)

The characterization and radiography of special nuclear materials (SNMs) such as plutonium and uranium is essential in various scenarios in the context of nonproliferation and national security. However, existing techniques are not sufficient in and of themselves for rapid isotope-sensitive interrogation of SNMs. In the present study, we propose an interrogation method, called scattering-nuclear-resonance-fluorescence-based computer tomography (SNRF CT), to reveal concealed SNMs with simultaneous measurements of the isotopic composition and tomographic distribution. Monte Carlo simulations show that three NRF signatures at 1802, 1846, and 1862 keV from a uranium target composed of ^{235}U and ^{238}U, irradiated by a quasimonochromatic γ-ray beam of high intensity, can be identified. For different target configurations, sinograms of the SNRF signatures are obtained, and the tomographic distributions are reconstructed with appreciable image contrast and spatial precision. It is found that the tomographic patterns of ^{235}U and ^{238}U hidden in a 30-mm-diameter iron rod can be clearly visualized. Compared with transmission NRF CT (TNRF CT), SNRF CT has the advantage that it does not need a witness target or calibration of the notch-refill effect. Furthermore, the imaging time for SNRF CT is 20 times shorter than that for TNRF CT, assuming a low missed-detection rate of 10^{-4}. We conclude that, using an intense γ-ray beam, the proposed SNRF CT technique is capable of simultaneous identification and tomographic imaging of the isotopic content of SNMs in a realistic measurement time. This imaging method could be extended to other applications in spent-fuel management and screening of cargo for explosives, drugs, and toxic chemicals.

DOI: 10.1103/PhysRevApplied.16.054048

I. INTRODUCTION

The illegal trafficking and criminal use of special nuclear materials (SNMs) such as plutonium and uranium is a great threat to national security and to nuclear-nonproliferation efforts [1,2]. Generally, the conventional x-ray scanning systems deployed at borders and ports of entry can acquire images that reveal only the density distribution of the measured object, and are not capable of differentiating SNMs from innocuous high-Z materials such as lead, tungsten, and bismuth. Consequently, efforts are being made to develop alternative ways to effectively detect SNMs and thus to prevent the smuggling of such substances. However, passive detection systems [3,4] utilizing the characteristic neutron or photon emissions of SNMs can be easily invalidated with proper shielding, since the intensity and energy of the emissions are fairly low. It is considered that active interrogation is an essential technique because of its promise of offering detection and characterization capabilities for SNMs in environments where passive detection fails.

Nuclear resonance fluorescence (NRF) [5–9]—the resonant absorption and reemission of photons by a nucleus—has been widely proposed as a powerful assay technique. Unlike techniques based on photon- or neutron-induced fission [10–16] or cosmic-ray muons [17–19], NRF can nondestructively provide isotopic signatures for SNMs without complicated spectrum analysis, dual- or multiple-energy beams, or large detection systems. It has been considered that bremsstrahlung-based NRF interrogation would deliver an unnecessary radiation dose to the object due to the wide energy spectrum of the interrogating beam. This problem can be remedied by using energy-tunable and quasimonochromatic γ-ray beams thanks to the development of laser-Compton scattering facilities [20], which have also been used for studies in nuclear physics [21,22] and nuclear astrophysics [23], and in industrial and medical applications [24–28]. Besides a

*wen.luo@usc.edu.cn and wenluo-ok@163.com

photon source that excites resonances, NRF techniques involve a measurement system that employs either transmission or scattering NRF (TNRF or SNRF) spectroscopy. In the former technique, one records NRF γ rays scattered from a witness target to measure the reduced spectral intensity of photons that have been resonantly absorbed, which allows physical encryption of sensitive information and thus has been applied in warhead verification [29,30]. The latter technique is based on the direct detection of NRF γ rays emitted from isotopes of interest; it provides high NRF counting rates and has been proposed for contraband identification [31–34] and ion thermometry [35]. Generally, the interrogation of SNMs requires the ability to resolve not only the isotopic composition but also the geometric makeup of suspicious nuclear species, making the development of NRF-based computer tomography (CT) important. In this context, the TNRF CT method has been proposed in order to measure tomographic images of high-density and high-Z objects [36,37]. However, the imaging process in TNRF CT is time-consuming, and simultaneous identification of multiple isotopes is difficult. Consequently, a rapid and efficient NRF-based imaging method is indispensable for addressing this issue.

In this paper, we propose and demonstrate a method, called SNRF CT, for rapid identification and simultaneous imaging of multi-isotope SNMs (see Fig. 1). It uses isotope-specific NRF emissions stimulated by an intense γ-ray source to identify isotopic components (^{235}U and ^{238}U) of SNMs. The isotopes of interest, emitting characteristic NRF signatures, can be regarded as distributed radioactive sources, whose spatial distributions are reconstructed using emission CT. The matrices of SNRF signatures resulting from target rotations and translations are simulated and incorporated into an image-reconstruction algorithm, generating isotope-specific tomographic images. Further analyses of the image contrast and accuracy are performed. Comparison against the TNRF CT method suggests that SNRF CT is able to simultaneously reveal the isotopic composition and spatial distribution of multi-isotope SNMs concealed in dense materials within a realistic interrogation time. Finally, the application of this method in other scenarios, including spent-fuel management and cargo screening, is discussed.

II. METHODS AND MATERIALS

To model the NRF interactions, we employ the G4NRF class from the Geant4-GENBOD toolkit [38,39], which has been benchmarked and used for studies of drug inspection and SNM interrogation [34,40]. In the simulations, a quasimonochromatic γ-ray source with a Gaussian energy distribution (with a centroid energy of 1854 keV and an energy spread of 1% in terms of standard deviation) and a photon intensity of 10^{10} photons/s is used for target irradiation; this can be delivered by state-of-the-art laser-Comton scattering (LCS) γ-ray sources [41,42]. Such a γ-ray beam can penetrate iron wrapping and interact with ^{235,238}U isotopes, triggering NRF reactions related to resonant states at 1846 keV (^{238}U) and 1862 keV (^{235}U). The widths of these resonant states are approximately 1 eV full width at half maximum (FWHM) and can be described by a Doppler-broadened Breit-Wigner formulation [5]. Specifically, the integral NRF cross sections at 1846 keV (^{238}U) and 1862 keV (^{235}U) are 23.0 ± 2.6 and 9.6 ± 0.7 eV b, respectively [43,44]. Two target configurations, i.e., scenarios I and II, are used to test the imaging performance. In scenario I, three 10-mm-diameter spheres made of uranium (80%

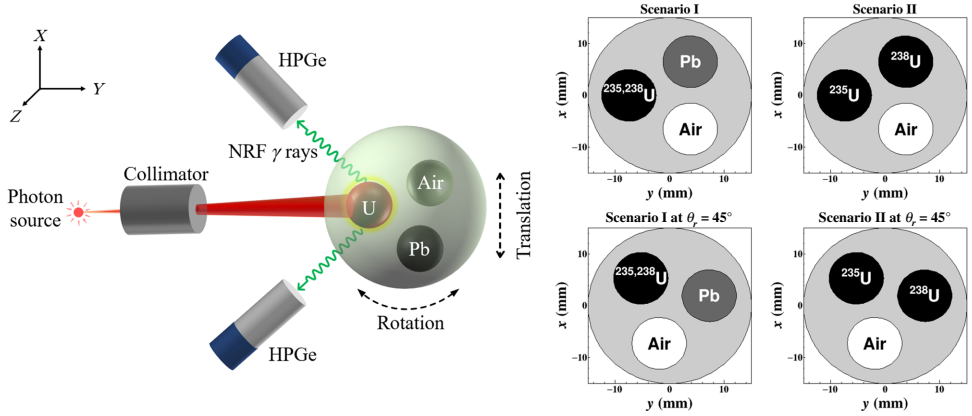

FIG. 1. Schematic illustration of isotope-sensitive imaging of SNMs. An intense γ-ray source irradiates an interrogation target with a diameter of 30 mm, which is placed 10 cm downstream of the γ-ray source. A collimator is used to select the quasimonochromaticity of the γ-ray source. The emitted NRF γ rays are detected by four high-purity germanium (HPGe) detectors, which are installed at backscattering angles with respect to the γ-ray propagation direction. The two detectors placed in the Y-O-Z plane are not shown, for brevity. Rotation and translation of the target enable acquisition of the projection data necessary for CT image reconstruction. The distance between the scanned object and the detectors is fixed at 22 cm.

^{235}U and 20% ^{238}U), lead, and air are enclosed in a 30-mm-diameter iron sphere. In scenario II, the materials of uranium and lead rods are replaced by 100% ^{235}U and 100% ^{238}U, respectively. The densities of uranium, lead, iron, and air are 19.1, 11.3, 7.8, and 1.3×10^{-3} g/cm^3, respectively.

The SNRF signatures resulting from target irradiation are recorded by four high-purity germanium (HPGe) detectors assembled at 135° relative to the beam propagation to take advantage of the decreasing intensity of nonresonantly backscattered radiation. The energy resolution of the HPGe detectors is assumed to be 0.1%, which is achievable with present detector technology. To acquire the projection data necessary for CT image reconstruction, the target is rotated (θ_r) about the Z axis in 32 steps of 11.2° and translated along the X axis (x) in 16 steps of 1.875 mm. In total, γ-ray spectra under 512 different conditions are obtained during the projection acquisition process.

In SNRF spectroscopy, one can use the NRF cross section, $\sigma_{\mathrm{NRF}}(E)$, and the angular distribution, $W(\theta)$, to construct a semianalytical expression for the expected NRF counts. For an interrogating photon beam of incident flux $I(E)$ interacting with the target, a small part of the photon flux near the resonant energy E_{NRF} undergoes resonant (NRF) and nonresonant (atomic) interactions inside the target. The resulting SNRF yield then produces a double-differential rate of NRF interactions in the infinitesimal solid angle $d\Omega$

$$\frac{d^2Y}{dE\,d\Omega} = I(E)\mu_{\mathrm{NRF}}(E)\frac{W(\theta)}{4\pi} \times \frac{1-\exp\left[-L\mu_{\mathrm{eff}}(E,E')\right]}{\mu_{\mathrm{eff}}(E,E')}\epsilon_d(E'), \quad (1)$$

where E and E' are the energies of the interrogating photons and scattered NRF photons, respectively, L is the thickness of the irradiated target, $\epsilon_d(E')$ is the intrinsic detection efficiency for the photopeak, $\mu_{\mathrm{NRF}}(E) = N\sigma_{\mathrm{NRF}}(E)$ denotes the linear attenuation coefficient, with N being the number density of the SNM target, and $\mu_{\mathrm{eff}}(E,E')$ is the effective attenuation coefficient, which is given by

$$\mu_{\mathrm{eff}}(E,E',\theta) = \mu_{\mathrm{NRF}}(E) + \mu_{\mathrm{nr}}(E) + \mu_{\mathrm{nr}}(E'). \quad (2)$$

Here $\mu_{\mathrm{nr}}(E)$ and $\mu_{\mathrm{nr}}(E')$ are the nonresonant attenuation coefficients for the interrogating photons and NRF photons, respectively.

The response of the detector to the SNRF signatures, represented as a matrix with respect to the rotation angle (θ_r) and translation length (x), $Y(x,\theta_r)$, is regarded as the projection data of the SNM distribution inside the target. According to the central slice theorem, all two-dimensional manifolds can be uniquely mapped from an infinite set of one-dimensional projections, although a finite set of projections is usually adequate in practice [45]. Consequently, it is feasible to reconstruct tomographic images of SNM isotopes from their projection matrices obtained from SNRF spectroscopy.

III. RESULTS

A. Isotopic identification

Figure 2 shows γ-ray spectra recorded by the HPGe detectors for the two target configurations at three rotation angles of 0°, 22.5°, and 45°. In scenario I, the SNRF signatures at 1802 keV (^{238}U), 1846 keV (^{238}U), and 1862 keV (^{235}U) can be observed simultaneously at 0°, with slightly stronger yields than those at 22.5°. Note that the 1802-keV line is a transition to the first excited state of ^{238}U from the resonant level at 1846 keV. The branching ratio for the 1846- and 1802-keV transitions is 100:51. At 45°, the SNRF signatures disappear due to the absence of ^{235,238}U in the pathway of the interrogating γ-ray beam. In scenario II, only the SNRF signature at 1862 keV (^{235}U) can be observed at rotation angles of 0° and 22.5°, while the signatures at 1802 keV (^{238}U) and 1846 keV (^{238}U) can be seen at 45°. Such a variation in the SNRF signatures indicates that the isotopic composition and the presence of SNMs can be probed, since these resonances are more than 10 keV apart, which prevents isotopic confusion and provides a one-to-one mapping between the energy and the identity of the materials.

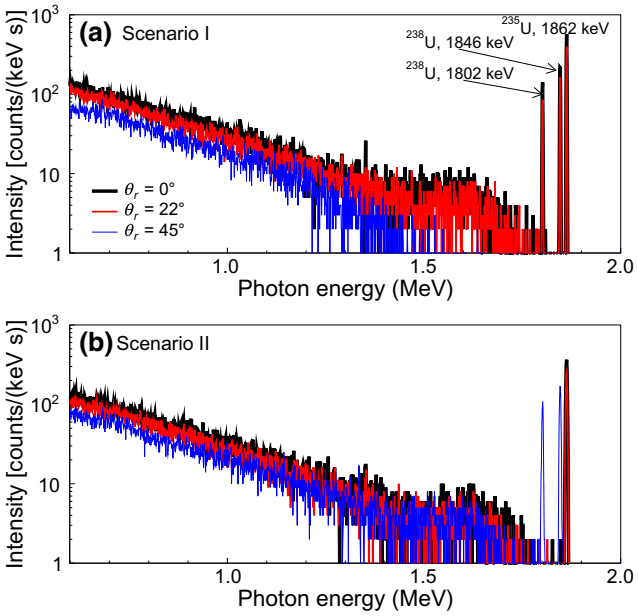

FIG. 2. Simulated NRF γ-ray spectra recorded by the HPGe scattering detectors at measurement points $(x,\theta_r) = (1.875\ \mathrm{mm}, 0°)$, $(1.875\ \mathrm{mm}, 22.5°)$, and $(1.875\ \mathrm{mm}, 45°)$ in scenario I (a) and scenario II (b) with 1 s irradiation.

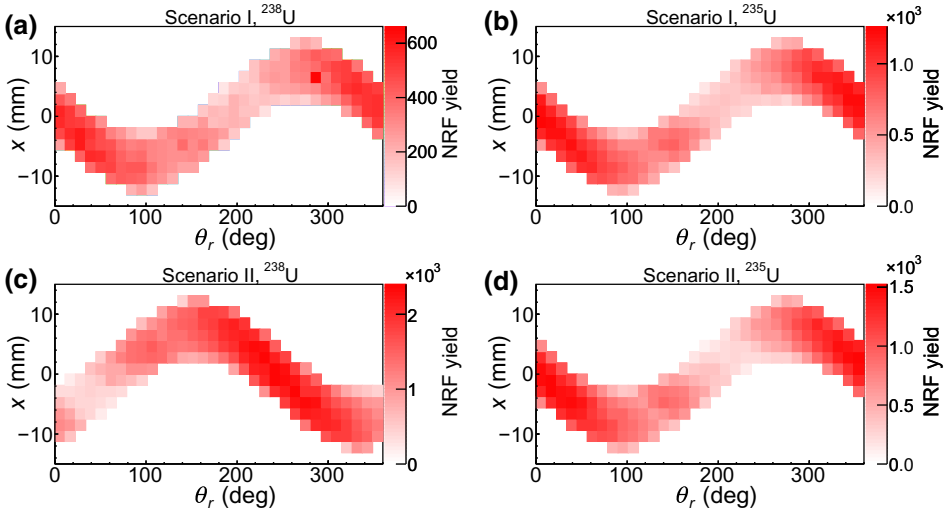

FIG. 3. Sinograms of the 1846-keV (^{238}U) SNRF signatures in scenario I (a) and scenario II (c). Sinograms of the 1862-keV (^{235}U) SNRF signatures in scenario I (b) and scenario II (d).

In order to further extract the SNRF yields from the spectra, the signal regions near 1802, 1846, and 1862 keV are then fitted with three Gaussian functions, on top of an exponentially decaying continuum background. The fitting function for these NRF peaks is written as

$$f(E) = \exp(c_1 + c_2 E) + \sum_{k=1}^{3} \frac{a_k}{\sqrt{2\pi}\sigma_k} \exp\left[-\frac{(E - E_k)^2}{2\sigma_k^2}\right], \tag{3}$$

where c_1 and c_2 describe the shape of the background, and a_k, E_k, and σ_k are the area, mean, and standard deviation of the kth peak and are fitting parameters.

Once the five-parameter fit for each NRF peak is computed using Eq. (3), the detected SNRF yields are extracted as simply $Y = a/\delta E$, where the division by the spectrum bin width δE enforces proper dimensions and normalization. Accordingly, the SNRF yields at 1862 keV (^{235}U) and 1846 keV (^{238}U) for different rotation angles and translation steps can be obtained, giving matrices of projection data for the image-reconstruction process (see Fig. 3). In scenario I, the sinogram of the 1862-keV (^{235}U) NRF line is similar to that of the 1846-keV (^{238}U) line. The NRF signal yields decrease as θ_r approaches approximately 220°; this is due to the fact that the attenuation of the lead rod becomes significant at these angles. In scenario II, the projection matrix of the 1846-keV NRF line is dissimilar to that for the 1862-keV line because of the disparate spatial distributions of ^{235}U and ^{238}U. With these projections, one can roughly infer the location and concentration of the nuclear species of interest embedded in the scanned object, but one is not yet able to acquire tomographic images of them.

B. Isotopic imaging

Tomographic images of SNMs can be reconstructed by incorporating the projection data into a filtered backprojection (FBP) algorithm. FBP is easy to implement, and is known for its computational efficiency and high accuracy with low-noise projection data with a substantial number of equiangularly distributed projection angles. Tomographic images of ^{235}U and ^{238}U reconstructed by FBP with a Hann filter for the two target configurations are shown in Fig. 4. In scenario I, the spatial distributions of ^{235}U and ^{238}U are similar, but the maximum SNRF yield reconstructed for the former is nearly twice as large as that for the latter. This is because the yield ratio $Y_{^{235}\mathrm{U}}/Y_{^{238}\mathrm{U}}$ is dependent not only on the isotope ratio (80:20) but also on the ratio of scattering NRF cross sections (9.6:15.2), the incident γ-ray intensity, the angular distribution, and the detection efficiency. In our case, the $Y_{^{235}\mathrm{U}}/Y_{^{238}\mathrm{U}}$ ratio is simulated to be 150:72, which is very close to the estimated

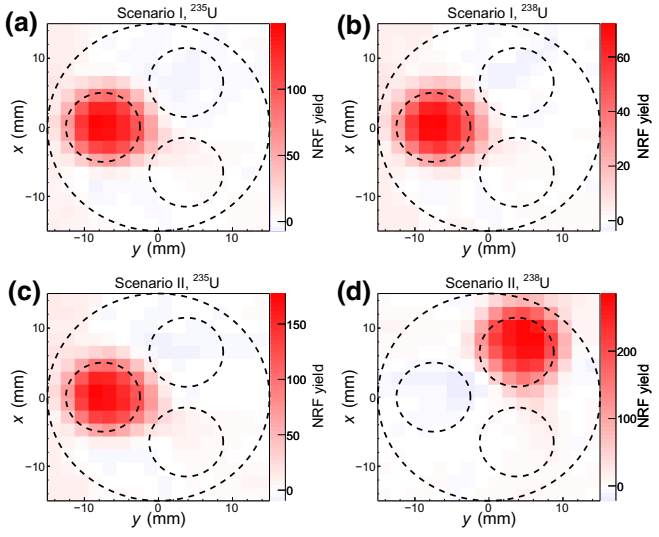

FIG. 4. Images reconstructed from sinograms of NRF signatures at 1862 keV (a) and 1846 keV (b) in scenario I. Images reconstructed from sinograms of NRF signatures at 1862 keV (c) and 1846 keV (d) in scenario II.

value (2.5) considering only the effect of the isotope ratio and the NRF cross-section ratio. In scenario II, the maximum NRF yield reconstructed for ^{235}U is close to that for ^{238}U; this is because the abundances of these two isotopes are both set to 100%. The reconstructed images show little sensitivity to the iron and lead materials, which cannot be distinguished well from SNMs using conventional x-ray CT due to their very close densities. These results show that SNRF CT is capable of revealing the spatial distribution of ^{235}U and ^{238}U and differentiating them from benign dense metals. In practice, inspectors could use this capability to verify the location of SNMs in a safeguards scenario, and emergency responders and armed-forces personnel could use this capability to isolate SNMs.

The contrast value of the signal within the uranium region with respect to the background can be defined by the following equation:

$$\text{Contrast} = \frac{|S - B|}{S + B}, \tag{4}$$

where S and B are the averaged reconstructed values of the 36 pixels in the ^{235}U-rod region and of the remaining pixels, respectively. The contrast values of the ^{235,238}U region for the two target configurations are calculated according to Eq. (4) and are shown in Table I. The contrast values of the ^{235,238}U region in scenario I and the ^{235}U region in scenario II are all 0.92, while that of the ^{238}U region in scenario II is 0.88. Such a high contrast indicates that the present technique is capable of producing images with reasonable quality and signal-to-noise ratio.

In order to further evaluate the imaging accuracy, we project the reconstructed images onto the x axis and calculate the relative count ratios P_i^x from

$$P_i^x = \frac{\sum_{j=0}^{16} R_{i,j}}{\max(\sum_{j=0}^{16} R_{i,j})}, \tag{5}$$

where $R_{i,j}$ is the SNRF count in the reconstructed image, i is the ith pixel along the x axis, j is the j th pixel along the y axis, and the sum over j denotes the projection onto the x axis. Likewise, the relative count ratios projected onto the y axis, P_j^y, can also be obtained. The resulting relative count-ratio distributions are compared with the original SNM distribution in Fig. 5. In the case of scenario I, the relative count-ratio distributions for ^{235}U and ^{238}U are similar for both the x and the y axis, and are consistent with the original region of the uranium rod in the target. However, the profile distributions of ^{238}U in scenario II are slightly shifted to the positive side of the x and y axes. This is due to the fact that the reconstruction accuracy of the FBP algorithm degrades in the case of a limited angular range, few projection angles, or a low signal-to-noise ratio.

TABLE I. Results for signal, background, and contrast values in each region of interest based on different target configurations.

Region	Signal	Background	Contrast
^{235}U (scenario I)	93.35	3.95	0.92
^{238}U (scenario I)	45.41	1.98	0.92
^{235}U (scenario II)	110.68	4.77	0.92
^{238}U (scenario II)	169.77	11.01	0.88

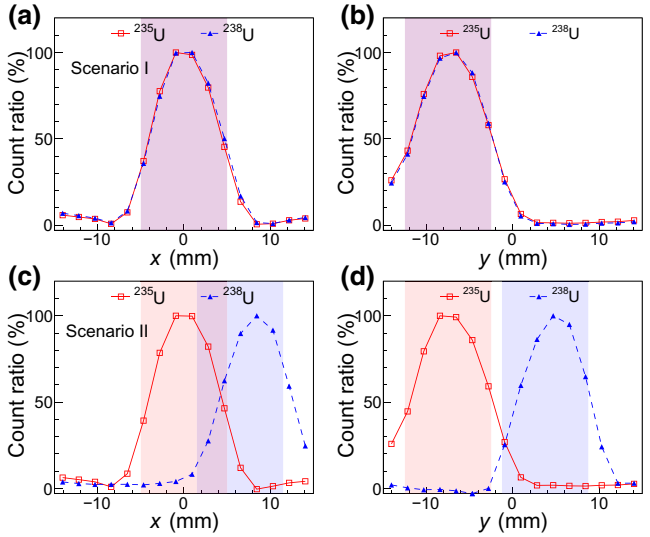

FIG. 5. Relative count ratios projected onto the x axis (a) and y axis (b) in scenario I, and projected onto the x axis (c) and y axis (d) in scenario II. The shaded areas represent the regions of the uranium rod.

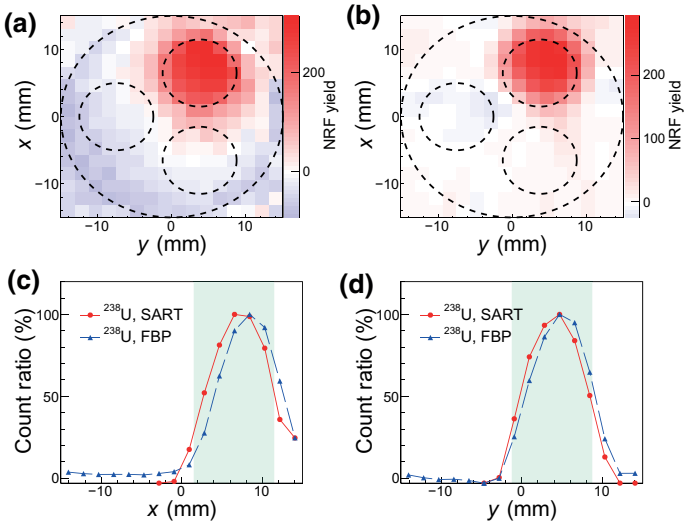

FIG. 6. Images of ^{238}U in scenario II reconstructed by the SART (a) and FBP (b) algorithms, and relative count ratios of the reconstructed images projected onto the x axis (c) and y axis (d). The shaded areas represent the regions of the uranium rod.

To address the misalignment issue, we apply the simultaneous-algebraic-reconstruction-technique (SART) algorithm [46] for image reconstruction. The resulting images, along with their relative count ratios, are shown in Fig. 6. Comparison shows that although the misalignment problem is solved in the SART image, there are more negative artifacts produced than in the FBP image. These results suggests that SART is successful in solving the misalignment problem, but has image-texture challenges with full strength due to the limited complexity of the model.

IV. DISCUSSION

Both SNRF CT and TNRF CT are capable of isotopic imaging, which is an essential feature for the assay of SNMs, since it can be used to characterize highly enriched uranium and plutonium. In SNRF CT, the reconstructed image represents the distribution of the source of NRF γ radiation in a plane within the object, whereas in TNRF CT it is a representation of the physical quantity governing the NRF attenuation coefficient in the material when the radiation beam traverses it and is detected on the other side. Despite their difference in physical connotations, images reconstructed from TNRF CT and SNRF CT can both reveal the geometric makeup of SNMs inside the scanned volume. When we use such images to infer the presence of SNMs in an interrogated volume, two types of errors can occur: a false alarm, where the test indicates that SNMs are present when in fact the "all clear" hypothesis is correct, and a missed detection, where the test shows "all clear" but SNMs are in fact present. In reality, it is absolutely essential to correctly classify every sample containing SNMs in order to minimize the risk of threatening international security, which highlights the importance of a low missed-detection rate.

For the reconstructed image of ^{235}U in scenario II, the significance of the ^{235}U signals can be expressed in units of σ as $\Delta_{\mathrm{SNRF}} = S/\delta S$, where δS is estimated from the averaged reconstructed value of the pixels outside the ^{235}U region. The variation of Δ_{SNRF} with the SNRF imaging time t_{SNRF} can be given as $\Delta_{\mathrm{SNRF}} = \Delta^0_{\mathrm{SNRF}} \times \sqrt{t_{\mathrm{SNRF}}/t^0_{\mathrm{SNRF}}}$, since the picture grain varies according to $1/\sqrt{D}$, with D being the dosage delivered by the interrogating beam [51]. In this case, we have $t^0_{\mathrm{SNRF}} = 512$ s, since the target is rotated and translated 512 times with an imaging time of 1 s each time to obtain the image of interest, and $\Delta^0_{\mathrm{SNRF}} = 23.0\sigma$ is obtained according to the values of S and δS extracted from the reconstructed image of ^{235}U in scenario II [see Fig. 4(c)]. To evaluate whether a measured object contains ^{235}U, the decision rule used is to alarm if Δ_{SNRF} exceeds a selected alarm threshold Δ_{th}. The probability that a measured object without ^{235}U is accidentally alarmed (false-alarm rate) because of random fluctuations can be given as $\alpha = 1 - [\Phi(\Delta_{\mathrm{th}}) - \Phi(-\Delta_{\mathrm{th}})]$, where Φ is the cumulative distribution function of the normal distribution centered at zero with variance unity [29]. From Δ_{SNRF}, the missed-detection rates can be readily calculated as $\beta_{\mathrm{SNRF}} = \Phi(\Delta_{\mathrm{th}} - \Delta_{\mathrm{SNRF}})$. To compare the resulting missed-detection rate with that for TNRF CT, we further generate a 16×16 image of ^{235}U in scenario II using the TNRF CT method. The detector assembly, witness-target configuration, and shielding arrangement are similar to those described in Ref. [40]. The photon beam used for target irradiation has a Gaussian energy distribution (with a centroid energy of 1862 keV and an energy spread of 1% in standard deviation) and a photon flux of 10^{10} photons/s. The image-reconstruction process is done by using FBP with a Hann filter. In this case, the variation of Δ_{TNRF} with the TNRF imaging time t_{TNRF} can be given analogously as $\Delta_{\mathrm{TNRF}} = \Delta^0_{\mathrm{TNRF}} \times \sqrt{t_{\mathrm{TNRF}}/t^0_{\mathrm{TNRF}}}$. Here $t^0_{\mathrm{TNRF}} = 257$ s, since the TNRF CT method requires 257 target scans to generate the image of interest, and $\Delta^0_{\mathrm{TNRF}} = 3.2\sigma$ is extracted from the reconstructed TNRF CT image. Using the same decision rule, the missed-detection rates can be evaluated as $\beta_{\mathrm{TNRF}} = \Phi(\Delta_{\mathrm{th}} - \Delta_{\mathrm{TNRF}})$.

Figure 7 shows the expected missed-detection rate β as a function of measurement time for cases using the SNRF CT and TNRF CT methods. For the case using TNRF CT, the imaging time required to reach a missed-detection rate of 10^{-4} is approximately 1200 s. This indicates that TNRF CT is able to detect all objects containing ^{235}U with greater than 99.99% probability in a 20-min scan. In comparison, the SNRF CT method requires only approximately 56 s to reach the same missed-detection rate; this is 20 times shorter than that required for TNRF CT.

Aside from the imaging time, the SNRF CT method has the advantage of being able to obtain spatial distributions of multiple isotopes simultaneously without the

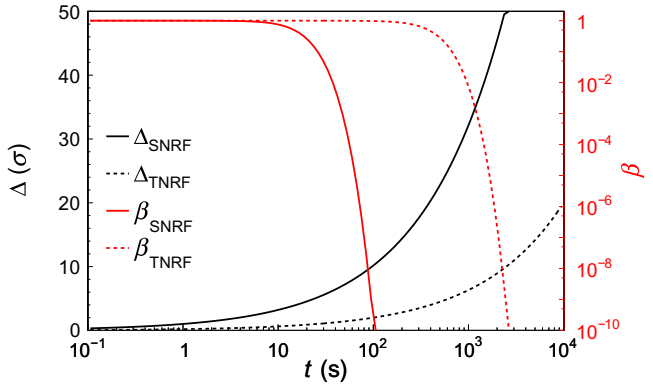

FIG. 7. Variation of Δ and β for cases using the TNRF CT method (dashed lines) and the SNRF CT method (solid lines) with an interrogation time t. An alarm threshold $\Delta_{\mathrm{th}} = 3.9\sigma$ is set for the calculations of β_{SNRF} and β_{TNRF} to achieve $\alpha = 10^{-4}$. The beam intensity is 10^{10} photons/s.

TABLE II. Resonant-state energy E_r, NRF γ-ray energy E_γ, branching ratio I_γ, level width Γ_0^2/Γ or Γ, integral NRF cross section σ_{int}, and imaging scenario for candidate isotopes suitable for SNRF CT imaging.

Isotope	E_r (keV)	E_γ (keV)	I_γ (%)	Γ_0^2/Γ or Γ (meV)	σ_{int} (eV b)	Imaging scenario
^{239}Pu	2040	2040	100	...	8.0 [47]	Nonproliferation and spent-fuel management
^{240}Pu	2156	2114	100	...	34.4 [48]	Nonproliferation and spent-fuel management
		2156	75			
^{232}Th	2043	1994	53	...	...	Nonproliferation and spent-fuel management
		2043	100	16.8	46.3 [49]	
^{237}Np	1729	1729	100	...	10.6 [50]	Spent-fuel management
^{12}C	4439	4438	100	10.8	6.3	Explosives and drug screening
^{14}N	7029	7027	~100	123.3	15.6	Explosives and drug screening
^{16}O	6917	6915	~100	97.1	38.9	Explosives and drug screening
^{31}P	3134	3134	~100	63.4	23.4	Toxic-chemical screening
^{32}S	2230	2230	100	26.9	103.9	Toxic-chemical screening

further consideration of manufacturing multi-isotope witness targets. Moreover, correction for the notch-refilling effect, which would erase the intensity of the NRF signature and result in less observed resonant attenuation [20,52,53], is no longer needed, since SNRF spectroscopy is applied. However, there are a few shortcomings that require further investigation. Firstly, the attenuation of SNRF γ rays in the scanned object has a negative effect on the detection of the SNRF signal, and needs to be corrected in order to obtain attenuation-free projection data and hence reconstruct SNM distributions more accurately. This is particularly important for the characterization of highly enriched uranium and plutonium, since the abundance of ^{235}U or ^{239}Pu can be deduced from the intensities of the SNRF signatures by using the isotope-ratio approach [34,40]. Secondly, the arrangement and collimation of the SNRF detectors must be optimized to meet the needs of the detection of typical emission CT signals.

Besides ^{235,238}U, SNRF CT can also be applied to imaging of other actinides such as ^{239,240}Pu, ^{232}Th, and ^{237}Np. These isotopes are also associated with nonproliferation and national-security work, and with spent-fuel management. Furthermore, the nuclear data on them required for SNRF CT studies have already been probed in previous NRF experiments [47–50]. Table II shows that the integral NRF cross sections of the 2040-keV (^{239}Pu), 2156-keV (^{240}Pu), 2043-keV (^{232}Th), and 1729-keV (^{237}Np) states are comparable to that of the 1846-keV (^{238}U) state chosen in the current study, which ensures sufficient SNRF yields for projection-data acquisition. The relatively high resonant energies also enable the interrogating and emitting photons to penetrate thick and dense shielding materials. Although there have been few recent NRF experiments regarding ^{12}C, ^{14}N, ^{16}O, ^{31}P, and ^{32}S, their integral NRF cross sections can still be derived from the Breit-Wigner formulas and level widths. Compared with the actinides, these light and medium isotopes generally have larger resonant energies and larger integral NRF cross sections, making it possible to use SNRF CT for screening of cargo for explosives, illicit drugs, and toxic chemicals.

It is also interesting to discuss the prospects for applying the SNRF CT method in realistic situations. Recently, Passport Systems, Inc., has developed a NRF-based detection system using bremsstrahlung radiation. This system was deployed at the Port of Boston for cargo screening [54]. With the rapid development of compact LCS γ-ray facilities [55–57], it is expected that it will be possible to perform such procedures using the SNRF CT method, although this requires a quasimonochromatic γ-ray beam rather than continuous bremsstrahlung radiation. Note that the photon energy required for SNM interrogation is typically below 3 MeV. Such photon beams of high intensity can be delivered by an LCS facility with a 532-nm laser and a 320-MeV electron accelerator.

In practical applications, a collimated γ-ray beam of sufficiently high intensity is generally needed to reduce the interrogation time, which may cause a pileup effect in the HPGe detectors. When the arrangement in scenario II is interrogated at a beam intensity of 10^{10} photons/s, the detector counting rates for both TNRF CT and SNRF CT are expected to be in the order of 10^5 s^{-1}. Such a counting rate is acceptable for commercially available HPGe detectors, since the time resolution of such detectors is at the microsecond level. To further avoid pileup effects, two possible approaches are suggested: (1) to increase appropriately the distance between the detector and the interrogated object while maintaining the total solid angle of the detector array, and (2) to install a lead foil in front of each detector, which can prevent a large number of low-energy background photons from hitting the detectors [58].

V. CONCLUSION

The characterization and detection of SNMs is an essential technique for nonproliferation and national security, and requires the capability to identify and image the isotopic composition of actinides. In this paper, we present

a NRF-based methodology for isotope-sensitive identification and tomographic imaging of concealed SNMs. Simulations show that the SNRF signatures of ^{235,238}U hidden in a 30-mm-diameter iron rod can be readily detected. The SNRF signatures at 512 measurement points are incorporated into a FBP algorithm to reconstruct isotope-sensitive tomographic patterns. It is found that the two-dimensional spatial distributions of ^{235}U and ^{238}U appear well defined in outline and tone. Compared with TNRF CT, the proposed SNRF CT technique has the advantage that it requires an interrogation time 20 times shorter, and without the need for preparation of a witness target or correction for the notch-refill effect. The SNRF CT technique can also be extended to identify and image other high-Z actinides and low-Z hazardous compounds, indicating potential for applications in spent-fuel management and screening of cargo for explosives, drugs, and toxic chemicals.

ACKNOWLEDGMENTS

This work is supported by the National Natural Science Foundation of China (Grant No. 11675075), the Youth Talent Project of Hunan Province, China (Grant No. 2018RS3096), and an independent research project of the Key Laboratory of Plasma Physics, CAEP (Grant No. JCKYS2020212006).

[1] C. D. Ferguson, W. C. Potter, and A. Sands, *The Four Faces of Nuclear Terrorism* (Routledge, 2005).

[2] IAEA, *Incident and Trafficking Database (ITDB) Incidents of nuclear and other radioactive material out of regulatory control, in 2020 Fact Sheet.* (International Atomic Energy Agency Vienna, Austria, New York, 2020).

[3] R. T. Kouzes, E. R. Siciliano, J. H. Ely, P. E. Keller, and R. J. McConn, Passive neutron detection for interdiction of nuclear material at borders, Nucl. Instrum. Methods Phys. Res. A **584**, 383 (2008).

[4] D. Cester, G. Nebbia, L. Stevanato, G. Viesti, F. Neri, S. Petrucci, S. Selmi, C. Tintori, P. Peerani, and A. Tomanin, Special nuclear material detection with a mobile multi-detector system, Nucl. Instrum. Methods Phys. Res. A **663**, 55 (2012).

[5] F. R. Metzger, Resonance fluorescence in nuclei, Prog. in Nuc. Phys. **7**, 54 (1959).

[6] T. Ogawa, S. Hashimoto, and T. Sato, Development of general nuclear resonance fluorescence model, J. Nucl. Sci. Technol. **53**, 1766 (2016).

[7] L. W. Faggand and S. S. Hanna, Polarization measurements on nuclear gamma rays, Rev. Mod. Phys. **31**, 711 (1959).

[8] K. Siegbahn, *Alpha-, beta-and gamma-ray spectroscopy*, Vol. 2 (North-Holland Amsterdam, Netherlands, 1965), p. 997.

[9] B. J. Quiter, *Nuclear resonance fluorescence for nuclear materials assay*, Ph.D. thesis, school UC Berkeley (2010).

[10] S. Finch, M. Bhike, C. Howell, W. Tornow, A. Tonchev, and J. Wilhelmy, *et al.*, Measurements of Short-Lived Isomers from Photofission as a Method of Active Interrogation for Special Nuclear Materials, Phys. Rev. Appl. **15**, 034037 (2021).

[11] J. Nattress, F. Sutanto, P. W. Fang, Y. Z. Chen, A. Cheng, K. Y. Chu, T. S. Duh, H. Y. Tsai, M. W. Lin, and I. Jovanovic, ^{1}2C(p, p')^{1}2C Reaction ($E_p = 19.5 - -30$ MeV) for Active Interrogation of Special Nuclear Material, Phys. Rev. Appl. **14**, 034043 (2020).

[12] J. Nattress, K. Ogren, A. Foster, A. Meddeb, Z. Ounaies, and I. Jovanovic, Discriminating Uranium Isotopes Using the Time-Emission Profiles of Long-Lived Delayed Neutrons, Phys. Rev. Appl. **10**, 024049 (2018).

[13] K. Ogren, J. Nattress, and I. Jovanovic, Discriminating Uranium Isotopes Based on Fission Signatures Induced by Delayed Neutrons, Phys. Rev. Appl. **14**, 014033 (2020).

[14] J. Zier, D. Mosher, R. Allen, R. Commisso, G. Cooperstein, D. Hinshelwood, S. Jackson, D. Murphy, P. Ottinger, and A. Richardson, *et al.*, High-power, photofission-inducing bremsstrahlung source for intense pulsed active detection of fissile material, Phys. Rev. ST Accel. Beams **17**, 060401 (2014).

[15] J. Petrović, A. Göök, and B. Cederwall, Rapid imaging of special nuclear materials for nuclear nonproliferation and terrorism prevention, Sci. Adv. **7**, eabg3032 (2021).

[16] B. S. Henderson, H. Y. Lee, T. D. MacDonald, R. G. Nelson, and A. Danagoulian, Experimental demonstration of multiple monoenergetic gamma radiography for effective atomic number identification in cargo inspection, J. Appl. Phys. **123**, 164901 (2018).

[17] J. M. Durham, D. Poulson, J. Bacon, D. L. Chichester, E. Guardincerri, C. L. Morris, K. Plaud-Ramos, W. Schwendiman, J. D. Tolman, and P. Winston, Verification of Spent Nuclear Fuel in Sealed dry Storage Casks via Measurements of Cosmic-Ray Muon Scattering, Phys. Rev. Appl. **9**, 044013 (2018).

[18] E. Guardincerri, J. Bacon, K. Borozdin, J. M. Durham, J. Fabritius II, A. Hecht, E. C. Milner, H. Miyadera, C. L. Morris, and J. Perry, *et al.*, Detecting special nuclear material using muon-induced neutron emission, Nucl. Instrum. Methods Phys. Res. A **789**, 109 (2015).

[19] P. Baesso, D. Cussans, J. Davies, P. Glaysher, C. Thomay, C. Vassallo, J. Velthuis, S. Quillin, S. Robertson, and C. Steer, High resolution muon tracking with resistive plate chambers, J. Instrum. **7**, P11018 (2012).

[20] number J. Pruet, D. P. Mcnabb, C. A. Hagmann, F. V. Hartemann, and C. P. J. Barty, Detecting clandestine material with nuclear resonance fluorescence, J. Appl. Phys. **99**, 123102 (2006).

[21] H. Utsunomiya, T. Renstrøm, G. Tveten, S. Goriely, T. Ari-Izumi, D. Filipescu, J. Kaur, Y. W. Lui, W. Luo, and S. Miyamoto, *et al.*, γ-ray strength function for thallium isotopes relevant to the ^{2}05Pb-^{2}05Tl chronometry, Phys. Rev. C **99**, 024609 (2019).

[22] M. C. Aianu, V. Derya, B. Loher, C. Matei, G. Pascovici, C. Petcu, C. Romic, D. Savran, G. Suliman, and E. Udup, *et al.*, Nuclear resonance fluorescence experiments at ELI-NP, Rom. Rep. Phys. **68**, S483 (2016).

[23] H. Y. Lan, Y. Xu, W. Luo, D. Balabanski, S. Goriely, M. La Cognata, C. Matei, A. Anzalone, S. Chesnevskaya, and G. Guardo, *et al.*, Determination of the photodisintegration

reaction rates involving charged particles: Systematic calculations and proposed measurements based on the facility for extreme light infrastructure–nuclear physics, Phys. Rev. C **98**, 054601 (2018).

[24] Z. C. Zhu, W. Luo, Z. C. Li, Y. M. Song, X. D. Wang, X. L. Wang, and G. T. Fan, Photo-transmutation of long-lived nuclear waste $^{1}35$Cs by intense Compton γ-ray source, Ann. Nucl. Energy **89**, 109 (2016).

[25] E. Irani, H. Omidvar, and R. Sadighi-Bonabi, Gamma rays transmutation of palladium by bremsstrahlung and laser inverse Compton scattering, Energ. Convers. Manage. **77**, 558 (2014).

[26] W. Luo, M. Bobeica, I. Gheorghe, D. M. Filipescu, D. Niculae, and D. L. Balabanski, Estimates for production of radioisotopes of medical interest at extreme light infrastructure–nuclear physics facility, Appl. Phys. B **122**, 8 (2016).

[27] W. Luo, D. L. Balabanski, and D. Filipescu, A data-based photonuclear simulation algorithm for determining specific activity of medical radioisotopes, Nucl. Sci. Tech. **27**, 113 (2016).

[28] W. Luo, Production of medical radioisotope $^{6}4$Cu by photoneutron reaction using ELI-NP γ-ray beam, Nucl. Sci. Tech. **27**, 96 (2016).

[29] R. S. Kemp, A. Danagoulian, R. R. Macdonald, and J. R. Vavrek, Physical cryptographic verification of nuclear warheads, Proc. Natl. Acad. Sci. U.S.A **113**, 8618 (2016).

[30] J. R. Vavrek, B. S. Henderson, and A. Danagoulian, Experimental demonstration of an isotope-sensitive warhead verification technique using nuclear resonance fluorescence, Proc. Natl. Acad. Sci. U.S.A **115**, 4363 (2018).

[31] O. Beck, T. Ruf, Y. Finkelstein, M. Cardona, T. Anthony, D. Belic, T. Eckert, D. Jäger, U. Kneissl, and H. Maser, *et al.*, Nondestructive determination of the $^{1}3$C content in isotopic diamond by nuclear resonance fluorescence, J. Appl. Phys. **83**, 5484 (1998).

[32] R. Hajima, N. Kikuzawa, N. Nishimori, T. Hayakawa, T. Shizuma, K. Kawase, M. Kando, E. Minehara, H. Toyokawa, and H. Ohgaki, Detection of radioactive isotopes by using laser Compton scattered γ-ray beams, Nucl. Instrum. Methods Phys. Res. A **608**, S57 (2009).

[33] D. Habsand and U. Köster, Production of medical radioisotopes with high specific activity in photonuclear reactions with γ-beams of high intensity and large brilliance, Appl. Phys. B **103**, 501 (2011).

[34] H. Y. Lan, T. Song, X. D. Huang, S. Q. Zhao, J. L. Zhou, Z. C. Zhu, Y. Xu, D. L. Balabanski, and W. Luo, Nuclear resonance fluorescence drug inspection, Sci. Rep. **11**, 1306 (2021).

[35] Y. Yuand and B. F. Shen, Ultrafast measurements of ion temperature in high-energy-density plasmas by nuclear resonance fluorescence, Phys. Plasmas **26**, 062708 (2019).

[36] I. Daito, H. Ohgaki, G. Suliman, V. Iancu, C. Ur, and M. Iovea, Simulation study on computer tomography imaging of nuclear distribution by quasi monoenergetic gamma rays with nuclear resonance fluorescence: Case study for ELI-NP application, Energy Procedia **89**, 389 (2016).

[37] H. Zen, H. Ohgaki, Y. Taira, T. Hayakawa, T. Shizuma, I. Daito, J. Yamazaki, T. Kii, H. Toyokawa, and M. Katoh, Demonstration of tomographic imaging of isotope distribution by nuclear resonance fluorescence, AIP Adv. **9**, 035101 (2019).

[38] S. Agostinelli, J. Allison, K. a. Amako, J. Apostolakis, H. Araujo, P. Arce, M. Asai, D. Axen, S. Banerjee, and G. Barrand, *et al.*, GEANT4 - a simulation toolkit, Nucl. Instrum. Methods Phys. Res. A **506**, 250 (2003).

[39] W. Luo, H. Y. Lan, Y. Xu, and D. L. Balabanski, Implementation of the n-body monte-carlo event generator into the geant4 toolkit for photonuclear studies, Nucl. Instrum. Methods Phys. Res. A **849**, 49 (2017).

[40] H. Y. Lan, T. Song, J. L. Zhang, J. L. Zhou, and W. Luo, Rapid interrogation of special nuclear materials by combining scattering and transmission nuclear resonance fluorescence spectroscopy, Nucl. Sci. Tech. **32**, 84 (2021).

[41] H. R. Weller, M. W. Ahmed, and Y. K. Wu, Nuclear physics research at the high intensity gamma-ray source (HIγS), Nucl. Phys. News **25**, 19 (2015).

[42] K. Tanaka, K. Spohr, D. Balabanski, S. Balascuta, L. Capponi, M. Cernaianu, M. Cuciuc, A. Cucoanes, I. Dancus, and A. Dhal, *et al.*, Current status and highlights of the ELI-NP research program, Matter Radiat. at Extremes **5**, 024402 (2020).

[43] E. Kwan, G. Rusev, A. S. Adekola, F. Dönau, S. L. Hammond, C. R. Howell, H. J. Karwowski, J. H. Kelley, R. S. Pedroni, R. Raut, A. P. Tonchev, and W. Tornow, Discrete deexcitations in $^{2}35$U below 3 MeV from nuclear resonance fluorescence, Phys. Rev. C **83**, 041601 (2011).

[44] A. Zilges, P. von Brentano, R.-D. Herzberg, U. Kneissl, J. Margraf, H. Maser, N. Pietralla, and H. H, Strong dipole excitations around 1.8 MeV in $^{2}38$U, Phys. Rev. C **52**, R468 (1995).

[45] V. Sharafutdinov, Uniqueness theorems for the exponential x-ray transform, J. Inverse Ill-Posed Probl. **1**, 355 (1993).

[46] A. H. Andersenand and A. C. Kak, Simultaneous algebraic reconstruction technique (SART): A superior implementation of the art algorithm, Ultrason. Imaging **6**, 81 (1984).

[47] W. Bertozzi, J. A. Caggiano, W. K. Hensley, M. S. Johnson, S. Korbly, R. Ledoux, D. P. McNabb, E. Norman, W. H. Park, and G. A. Warren, Nuclear resonance fluorescence excitations near 2 MeV in $^{2}35$U and $^{2}39$Pu, Phys. Rev. C **78**, 041601 (2008).

[48] B. J. Quiter, T. Laplace, B. A. Ludewigt, S. D. Ambers, B. L. Goldblum, S. Korbly, C. Hicks, and C. Wilson, Nuclear resonance fluorescence in $^{2}40$Pu, Phys. Rev. C **86**, 034307 (2012).

[49] A. Adekola, C. Angell, S. Hammond, A. Hill, C. Howell, H. Karwowski, J. Kelley, and E. Kwan, Discovery of low-lying E1 and M1 strengths in $^{2}32$Th, Phys. Rev. C **83**, 034615 (2011).

[50] C. T. Angell, R. Yee, T. Joshi, E. Swanberg, E. Norman, C. Hicks Jr, A. Klimenko, S. Korbly, C. Wilson, and W. Kulp, *et al.*, Nuclear resonance fluorescence of $^{2}37$Np, Phys. Rev. C **82**, 054310 (2010).

[51] G. N. Hounsfield, Picture quality of computed tomography, AJR Am. J. Roentgenol. **127**, 3 (1976).

[52] C. Hagmann, J. Hall, M. Johnson, D. McNabb, J. Kelley, C. Huibregtse, E. Kwan, G. Rusev, and A. Tonchev, Transmission-based detection of nuclides with nuclear

resonance fluorescence using a quasimonoenergetic photon source, J. Appl. Phys. **106**, 084901 (2009).

[53] B. J. Quiter, B. A. Ludewigt, V. V. Mozin, C. Wilson, and S. Korbly, Transmission nuclear resonance fluorescence measurements of $^{2}38$U in thick targets, Nucl. Instrum. Methods Phys. Res. B **269**, 1130 (2011).

[54] Improved threat-detection, https://news.mit.edu/2016/startup-improved-nuclear-threat-detection-0622 (accessed on 1 October 2021).

[55] F. Albert, S. Anderson, D. Gibson, C. Hagmann, M. Johnson, M. Messerly, V. Semenov, M. Shverdin, B. Rusnak, and A. Tremaine, *et al.*, Characterization and applications of a tunable, MeV-class Compton-scattering γ-ray source, laser-based, Phys. Rev. ST Accel. Beams **13**, 070704 (2010).

[56] T. Akagi, A. Kosuge, S. Araki, R. Hajima, Y. Honda, T. Miyajima, M. Mori, R. Nagai, N. Nakamura, and M. Shimada, *et al.*, Narrow-band photon beam via laser Compton scattering in an energy recovery linac, Phys. Rev. Accel. Beams **19**, 114701 (2016).

[57] Z. L. Pan, J. Byrd, H. Hao, W. H. Huang, D. R. Li, C. C. Sun, Y. K. Wu, and C. X. Tang, Design and dynamic studies for a compact storage ring to generate γ-ray light source based on Compton backscattering technique, Phys. Rev. Accel. Beams **22**, 040702 (2019).

[58] W. Luo, T. P. Yu, M. Chen, Y. M. Song, Z. C. Zhu, Y. Y. Ma, and H. B. Zhuo, Generation of bright attosecond x-ray pulse trains via Thomson scattering from laser-plasma accelerators, Opt. Express **22**, 32098 (2014).